Applied Physics A (2019) 125:704
https://doi.org/10.1007/s00339-019-3003-0

Applied Physics A
Materials Science & Processing

Substrate temperature dependent physical properties of $SnS_{1-x}Se_x$ thin films

K. Saritha[1] · S. Rasool[1] · K. T. Ramakrishna Reddy[1] · A. M. Saad[2] · M. S. Tivanov[3] · S. E. Tikoto[3] · O. V. Korolik[3] · V. F. Gremenok[4]

Received: 18 July 2019 / Accepted: 10 September 2019

Abstract
Recently, researchers showed great interest on $SnS_{1-x}Se_x$ alloy films because of their tunable physical properties that are suitable as an absorber layer in thin film solar cells. In the present work, $SnS_{1-x}Se_x$ thin films were deposited by thermal co-evaporation of SnS and Se at different substrate temperatures ranging from 200 to 350 °C. The influence of substrate temperature (T_s) on composition, structure, surface morphology, topography and optical properties of as-deposited films was investigated using appropriate techniques and the results are reported in detail. The EDS analysis of $SnS_{1-x}Se_x$ films showed that Sn/(S + Se) ratio was changed from 0.84 to 1.16 with increase of substrate temperature. All the films were polycrystalline in nature, exhibiting (111) plane as preferred orientation with orthorhombic crystal structure. From W–H analysis, the crystallite size and lattice strain in the films were evaluated, where the crystallite size varied in the range, 9–22 nm with substrate temperature. The layers showed a change in the shape of grains with the rise of substrate temperature, where the grain size has increased with T_s. The topographical results indicated an indirect relation between surface roughness and average grain size with change in substrate temperature. The band gap energy values of the films was decreased with increase of T_s and varied in the range, 1.59–1.46 eV. In addition, the photoconductivity measurements revealed that the as-deposited $SnS_{1-x}Se_x$ films had bimolecular type recombination ($\gamma \sim 0.5$) of photo-generated charge carriers.

1 Introduction

In recent years, many research groups have been working on tin based chalcogenide materials for optoelectronic device applications. Among them, SnS and SnSe are promising light absorbing materials used for low cost thin film solar cell applications owing to their earth abundance, less toxicity of constituent elements and favourable physical properties. Both these materials showed high optical absorption coefficient ($\sim 10^5$ cm^{-1}) and tunable optical band gap energy (1–2 eV) [1–6]. Moreover, both SnS and SnSe are p-type semiconductors exhibiting orthorhombic crystal structure with optical band gaps of 1.3 eV and 1.0 eV respectively [7–9]. Though they are efficient materials for solar energy conversion, however, the reported conversion efficiencies are low (SnS—4.63% and SnSe—≤ 1%) [10, 11]. Particularly, the reported theoretical conversion efficiency is 33% for SnS based solar cells, that is very much higher than that achieved at present [12]. Moreover, pure sulfide and selenide based solar cells showed less conversion efficiency as in the case of quaternary materials like CZTS (9.2%) and CZTSe (11.6%) than mixed sulfo-selenide based solar cells, CZTSSe (12.6%) [13]. In this context, tin sulfoselenide (SnSSe) has received more attention due to its adequate environmental stability and possibility to alter the optical and electrical properties according to the amount of S and Se content in the films. SnSSe is a p-type semiconductor, possessing the properties of both SnS and SnSe.

As per the literature survey, the reports available on the synthesis and characterization of SnSSe are meagre. Till now, few chemical and physical deposition techniques have been employed to prepare $SnS_{1-x}Se_x$ in different forms such as single crystals, nanocrystals, nanosheets and thin films.

✉ K. T. Ramakrishna Reddy
ktrkreddy@gmail.com

[1] Solar Photovoltaic Laboratory, Department of Physics, Sri Venkateswara University, Tirupati 517 502, India

[2] Al-Balqa Applied University, PO Box 4545, Amman 11953, Jordan

[3] Faculty of Physics, Belarusian State University, 220030 Minsk, Belarus

[4] Scientific and Practical Materials Research Centre, National Academy of Sciences, 220072 Minsk, Belarus

Published online: 17 September 2019

Table 1 presents the list of research articles reported in literature on p-type $SnS_{1-x}Se_x$ and the parameters investigated, including few reports on solar cell parameters. It can be seen from the table that although few studies have been reported mainly on the structure and optical properties of $SnS_{1-x}Se_x$ films deposited by different methods, the research on material properties of $SnS_{1-x}Se_x$ films lack coherence in presentation of results mapping onto the deposition conditions. Hence, a systematic and detailed investigation on the material properties in relation to the growth conditions are highly essential to optimize the deposition parameters for the development of efficient $SnS_{1-x}Se_x$ based thin film solar cells.

The present work deals with the deposition of $SnS_{1-x}Se_x$ thin films by thermal co-evaportion technique, which is a suitable approach to prepare compound or alloy materials in thin film form. As per literature survey, no reports are available on thermally co-evaporated $SnS_{1-x}Se_x$ films. In vacuum techniques, substrate temperature is one of the important parameters to be optimized to grow high quality films. Hence, the aim of this work is to investigate the effect of substrate temperature on the composition, structure, morphology, topography, optical and photosensitivity of thermally co-evaporated $SnS_{1-x}Se_x$ films and optimize the substrate temperature to obtain good quality films.

Table 1 Literature survey and material properties of p-type $SnS_{1-x}Se_x$ phase

S. no.	Phase	Form	Preparation method	Crystal structure	Band gap energy, E_g (eV)	Solar cell parameters	Year and References
1	$SnS_{1-x}Se_x$	Single crystals	Melt quenching	Orthorhombic	1.08–0.90	–	1962, [14]
2	SnS_xSe_{1-x}	Single crystals	Direct vapour transport	Orthorhombic	–	–	2003, [15]
3	$SnS_{0.5}Se_{0.5}$	Thin films	Electro- deposition	Orthorhombic	1.1	V_{oc} = 0.23–0.24 V; I_{sc} = 1.55–1.63 mA; $\eta < 1\%$	2003, [16]
4	SnS_xSe_{1-x}	Nano crystals	Hot injection method	Orthorhombic	0.92–1.24	–	2011, [17]
5	SnSSe	Thin films	Electro- deposition	Orthorhombic	1.08–1.25	–	2011, [18]
6	SnS_xSe_{1-x}	Nano crystals	Pulsed laser deposition	Orthorhombic	1.06	–	2013, [19]
7	SnS_xSe_{1-x}	Thin films	Cathodic potentiostatic method	Orthorhombic	1.08	–	2015, [20]
8	SnS_xSe_{1-x}	Thin films	Chemical bath deposition	Cubic	1.52	–	2016, [21]
9	$SnSe_{1-x}S_x$	Nanosheets	Hydrothermal-chemical exfoliation	Orthorhombic	–	–	2017, [22]
10	$SnSe_{1-x}S_x$	Single crystals	Temperature gradient growth method	Orthorhombic	–	–	2017, [23]
11	$SnS_{1-x}Se_x$	Solid solution	Mechanical alloying & spark plasma sintering	Orthorhombic	–	–	2017, [24]
12	$SnS_{0.65}Se_{0.35}$	Thin films	Chemical bath deposition	Cubic	1.52	V_{oc} = 496 mV; J_{sc} = 7.5 mA/cm^2; η = 1.15%	2017, [25]
13	$SnS_{1-x}Se_x$	Thin films	Electro-deposition	Orthorhombic	1.22–1.65	–	2017, [26]
14	$SnSe_{0.8}S_{0.2}$	Porous nanosheets	Hydrothermal-chemical exfoliation	Orthorhombic	–	–	2018, [27]
15	$SnSe_{1-x}S_x$	Solid solutions	Cluster expansion	Orthorhombic	–	–	2018, [28]
16	$SnS_{1-x}Se_x$	Nanosheets	Physical vapour deposition	Orthorhombic	–	–	2018, [29]
17	$SnS_{0.5}Se_{0.5}$	Thin films	Screen printing	Orthorhombic	1.21	–	2018, [30]
18	$SnS_{0.4}Se_{0.6}$	Thin films	Thermal evaporation	Orthorhombic	1.25–1.02	–	2018, [31]
19	$SnS_{1-x}Se_x$	Thin films	Electrochemical deposition	Orthorhombic	1.4	V_{oc} = 160 mV; J_{sc} = 2.7 μA/cm^2; $\eta = 1.6 \times 10^{-4}$ %	2018, [32]
20	$SnS_{1-x}Se_x$	Thin films	Thermal co-evaporation	Orthorhombic	1.59–1.46	–	Present work

2 Experimental and characterization details

2.1 Preparation of $SnS_{1-x}Se_x$ thin films

Thermal co-evaporation technique (HHV model BC 300 box coater) was employed to deposit $SnS_{1-x}Se_x$ thin films using SnS (Alfa Aesar, 99.5%) and elemental Se (Sigma Aldrich, 99.99%) as source materials. $SnS_{1-x}Se_x$ layers were deposited onto ultrasonically cleaned and preheated soda lime glass substrates through co-evaporation at a vacuum of 5×10^{-5} mbar at varied substrate temperatures (T_s) ranging from 200 to 350 °C. The deposition temperature was chosen in this range because the films grown at temperatures < 200 °C were of porous in nature and also not well adherent to the substrate surface. Further, the films formed above 350 °C were highly sulphur/selenium deficient owing to its high vapour pressure at such temperatures and the layers were highly reflecting in visual appearance. So, the substrate temperature was chosen in the range of 200–350 °C. Moreover, a circular type radiant heater of 1 kW was used to heat the substrate holder to required temperature. A K-type thermocouple was placed near the substrate holder to measure the temperature and a proportional integral derivative (PID) controller was used to control the substrate holder temperature. The other deposition parameters such as source to substrate distance and evaporation rate were kept constant as 13 cm and 20 Å/s respectively for all depositions, while the thickness of the as-deposited films was maintained approximately as 1 µm, measured by quartz crystal thickness monitor (model CTM-200).

2.2 Characterization details

The structural properties of as-deposited $SnS_{1-x}Se_x$ films was analysed by Ultima-IV X-ray diffractometer in grazing incidence diffraction (GIXRD) geometry at 1 degree of incident X-rays with Cu Kα radiation source ($\lambda = 1.5406$ Å). Diffraction angle in the range, 10–70° was used to identify the crystal planes present in the films and to evaluate other structural parameters. The structural phases present in the films were analysed by Raman spectroscopy using Nanofinder HE confocal Raman spectrometer performed at room temperature in the back scattering configuration, a solid state laser of wavelength 532 nm was used as a light source. Optical power incident on the samples was reduced down to 60 µW to avoid their damage. The × 100 objective lens (NA = 0.95) provided size of excitation spot of about 0.7 µm. Raman spectra were obtained with a spectral resolution better than 3.0 cm^{-1}. The surface morphology and the chemical composition of the as-deposited films were investigated using scanning electron microscope (SEM) (S-4800, Hitachi) attached with energy dispersive X-ray spectroscopy (EDS) (Oxford Instruments, Inca Penta FET × 3). The surface topography of the films were analyzed using atomic force microscopy (AFM) (Solver Nano, NT-MDT). The AFM instrument was used in semi-contact mode with a scanning probe of 10 nm tip radius at a resonance frequency of 227 kHz. Photon RT spectrophotometer (Essent Optics) was used to analyze the optical properties of the layers using unpolarized light at room temperature. Moreover, the photoconductivity of the films was measured at a constant temperature of 307 K under LED illumination with excitation wavelength of 465 nm.

3 Results and discussion

Thermally co-evaporated $SnS_{1-x}Se_x$ films were appeared to be pale bluish grey in colour, uniform, pinhole free and the scratch tape test revealed that the layers were well adherent to the substrate surface.

3.1 EDS analysis

The elemental composition analysis of as-deposited films was carried out using energy dispersive X-ray spectroscopy (EDS). The EDS analysis revealed the presence of Sn, S and Se as constituent elements in all the as-deposited films. A typical EDS spectrum of $SnS_{1-x}Se_x$ thin films deposited at $T_s = 300$ °C was shown in Fig. 1. The atomic percentages of constituent elements in the as-deposited films and the variation in Sn/(S + Se) ratio with substrate temperature are listed in Table 2. It is observed from the table that increase of substrate temperature made the films Sn-rich and Sn/(S + Se) ratio increased with T_s. The variations in Sn/(S + Se) ratio might be due to variations in the vapour pressures of constituent elements. With raise of substrate temperature, S and Se contents were decreased due to re-evaporation, which is a common phenomenon that occurs in thermal methods at higher temperatures. This kind of re-evaporation of chalcogenides (Se/S) from the film surface was reported by various researchers in the literature on different chalcogenide materials [33–36].

3.2 Structural properties

Figure 2 shows the GIXRD patterns of $SnS_{1-x}Se_x$ thin films deposited at different substrate temperatures that vary in the range, 200–350 °C. All the films exhibited an intense peak at $2\theta = 31.7°$ that corresponds to the (111) plane of the orthorhombic crystal structure. The other peaks present in the films were identical to the planes

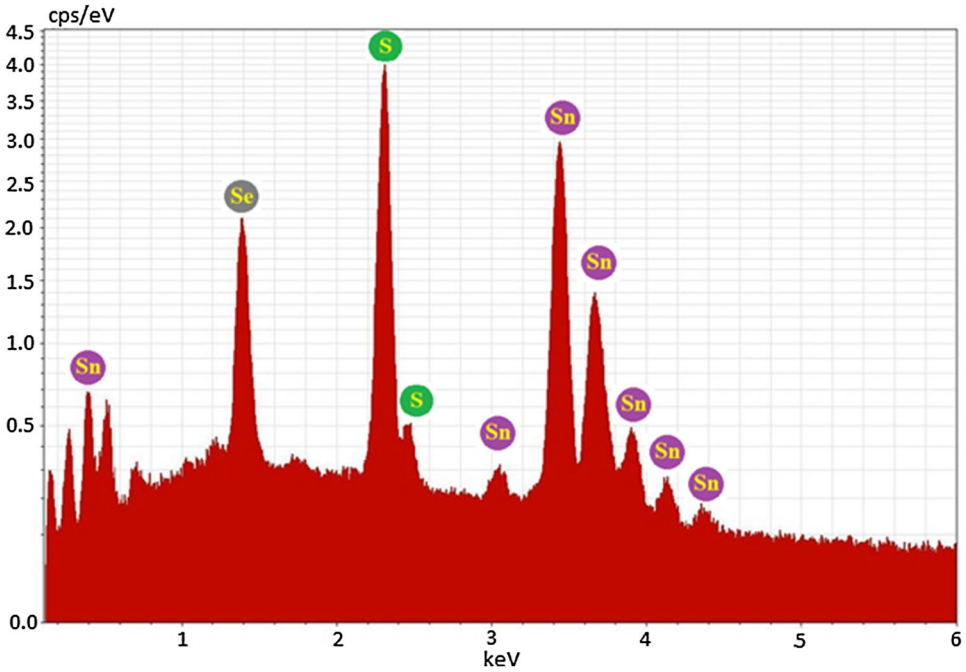

Fig. 1 EDS spectrum of $SnS_{1-x}Se_x$ thin films deposited at $T_s = 300$ °C

Table 2 Atomic percentages of $SnS_{1-x}Se_x$ thin films deposited at different substrate temperatures

T_s (°C)	Sn (at.%)	S (at.%)	Se (at.%)	Sn/(S + Se)	Compound
200	45.8	40.1	14.1	0.84	$SnS_{0.74}Se_{0.26}$
250	51.3	35.1	13.6	1.05	$SnS_{0.72}Se_{0.28}$
300	51.5	34.0	14.5	1.06	$SnS_{0.70}Se_{0.30}$
350	53.7	32.0	14.3	1.16	$SnS_{0.69}Se_{0.31}$

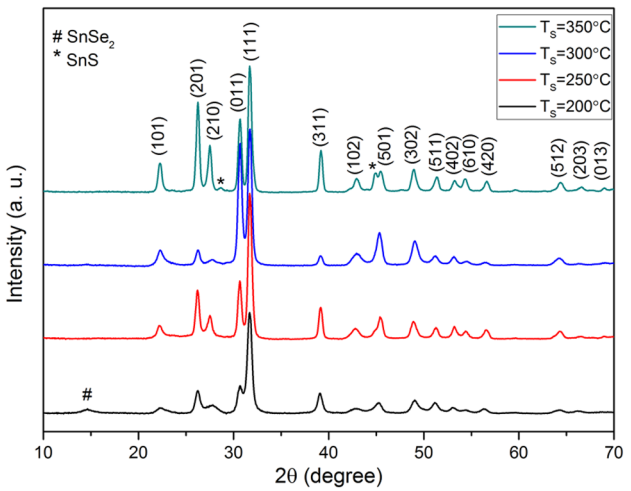

Fig. 2 The GIXRD patterns of $SnS_{1-x}Se_x$ thin films prepared at different substrate temperatures

reported for the ternary $SnS_{1-x}Se_x$ ($x = 0.5$) crystal phase available in the JCPDS card No. 48-1225. Further, all the peaks observed in this work are similar to those reported by Han et al. for $SnS_{1-x}Se_x$ solid solutions [37]. This confirmed the formation of ternary chalcogenide $SnS_{1-x}Se_x$ phase in the films grown in this work.

Figure 2 shows the effect of change in substrate temperature on the intensity and sharpness of the diffraction peaks, which in turn gives information on crystallinity of the films. At $T_s = 200$ °C, a small $SnSe_2$ peak was observed at $2\theta = 14.6°$ along with $SnS_{1-x}Se_x$ phase. This was probably due to the insufficient thermal energy required to form the ternary phase at such temperatures. However, with an increase of substrate temperature to 250 °C, the $SnSe_2$ peak disappeared and only $SnS_{1-x}Se_x$ phase was observed. At $T_s = 300$ °C, the intensity of peaks corresponding to the ternary phase was increased and became sharp, representing homogeneity and good crystallinity of the films. This indicated that Se and SnS phases reacted together at such temperatures to form the ternary phase with larger crystallite size. For further increase of temperature to 350 °C, SnS peaks were observed as secondary phase along with $SnS_{1-x}Se_x$ phase. This might be due to either dissociation of part of the ternary phase into stable binary SnS phase by re-evaporating Se or desorption of Se atoms at such higher temperatures. Such presence of secondary phases were also observed by Banotra et al. for $SnS_{0.4}Se_{0.6}$ alloy films annealed at higher temperatures [31].

The inter-planar spacing (d) between the crystal planes of as-grown $SnS_{1-x}Se_x$ layers was calculated for the (111) plane using Bragg's diffraction law (relation 1), where θ is the diffraction angle. The unit cell dimensions of orthorhombic structure, a, b and c values were evaluated using (101), (011) and (111) planes by following the

relation (2). The unit cell volume (V) of the films was calculated using relation (3).

$$d_{hkl} = \frac{\lambda}{2\sin\theta} \tag{1}$$

$$\frac{1}{d^2} = \frac{h^2}{a^2} + \frac{k^2}{b^2} + \frac{l^2}{c^2} \tag{2}$$

$$V = abc \tag{3}$$

All the calculated lattice parameters of $SnS_{1-x}Se_x$ films as a function of substrate temperature are listed in Table 3. It was noticed that the lattice parameters varied with increase of substrate temperature. A similar type of variation in lattice parameters in thermally evaporated $SnS_{0.4}Se_{0.6}$ films was reported by Banotra et al. [31].

The microstructural parameters of $SnS_{1-x}Se_x$ films such as crystallite size (D) and lattice strain (ε) were calculated in the present work using Williamson–Hall (W–H) method. The W–H analysis is a simplified integral breadth method, where both size and strain induces broadening of X-ray peaks [36]. Moreover, it is more suitable method to determine crystallite size than the Debye–Scherrer method, because of the consideration of strain developed in the films also for the GIXRD peak broadening (β). The W–H equation in uniform deformation model (UDM), where the strain is assumed to be uniform in all crystallographic directions, is given by the relation (4) [38].

$$\beta\cos\theta = \frac{k\lambda}{D} + 4\varepsilon\sin\theta \tag{4}$$

Figure 3a–d shows the W–H plots of as-deposited $SnS_{1-x}Se_x$ films.

Seven most intensive peaks have been used to obtain crystal parameters by W–H approach. The estimated values of average crystallite size (D) and lattice strain (ε) from the W–H analysis of $SnS_{1-x}Se_x$ films with respect to change of substrate temperature were shown in Fig. 4a, b. It is observed from Fig. 4a that the crystallite size is increased with increase of T_s and reached a maximum of 22 nm at $T_s = 300$ °C and then decreased with further rise in substrate temperature due to re-evaporation of S/Se from the film surface and/or reduction in film—substrate surface interaction as observed in case of In_2S_3 films [39]. Figure 4b demonstrates that the strain in the films is compressive with negative slope at $T_s = 200$ °C and then increased to positive slope indicating tensile strain in the films at higher T_s. Further, it can be noted from Fig. 4b that the lattice strain increases with the increase of substrate temperature, in contrary to the general trend observed in different thin films. This can be explained as follows. With increase of T_s, the Se-content in the layers was increased because of the re-evaporation of S from film surface, owing to its high vapour pressure, while the film surface is exposed to continuous influx of Sn, S and Se atoms from the sources. This resulted in the occupation of vacant S sites by Se atoms. As Se ionic radius (1.98 Å) is higher than S ionic radius (1.84 Å), replacement of S vacancies by Se atoms led to lattice distortion and increased unit cell volume (as noted from Table 3), causing lattice strain that increases with increase of T_s up to 300 °C. However, the reduced lattice strain at $T_s = 350$ °C might be due to re-evaporation of both S and Se from the film surface, causing less distortion in the lattice.

3.3 Raman analysis

Figure 5 shows the Raman modes obtained for $SnS_{1-x}Se_x$ films grown at different substrate temperatures, given in the range of 50–400 cm^{-1}. The deconvolution of peaks done by the Lorentz approximation showed the presence of various optical phonon modes inherent to SnS and SnSe phases in the spectra. It was observed that the Raman modes in the regions of 106-110 cm^{-1}, 133 cm^{-1}, 147/150 cm^{-1} correspond to SnSe, and those present at 119 cm^{-1}, 185 cm^{-1} to $SnSe_2$. Further, the relative intensities of these modes decreases with increase of substrate temperature. Similarly, the modes observed in the regions of 90 cm^{-1}, 123 cm^{-1}, 174/176 cm^{-1}, 202 cm^{-1} are attributed to SnS, where the relative intensities are also decreases with increase of T_s, while the modes present at 95/97 cm^{-1}, 160 cm^{-1}, 191 cm^{-1}, 220 cm^{-1} are related to SnS became more intense. In addition, with increase of the substrate temperature, a decrease in the width of modes appeared at 95/97 cm^{-1}, 191 cm^{-1}, 220 cm^{-1} is observed. Another intense mode observed at 183/185 cm^{-1} can be matched with both $SnSe_2$ and SnS. Further, it should be noted that in the region of 305–312 cm^{-1},

Table 3 The lattice parameters of $SnS_{1-x}Se_x$ thin films

T_s (°C)	2θ (°)	*(hkl)*	Lattice constants {(101), (011) and (111)}			Unit cell volume (Å^3)
			a (Å)	*b* (Å)	*c* (Å)	
200	31.70	(111)	11.35	3.99	4.29	194
250	31.72	(111)	11.36	3.98	4.32	195
300	31.73	(111)	11.38	3.99	4.34	197
350	31.73	(111)	11.35	4.01	4.31	196

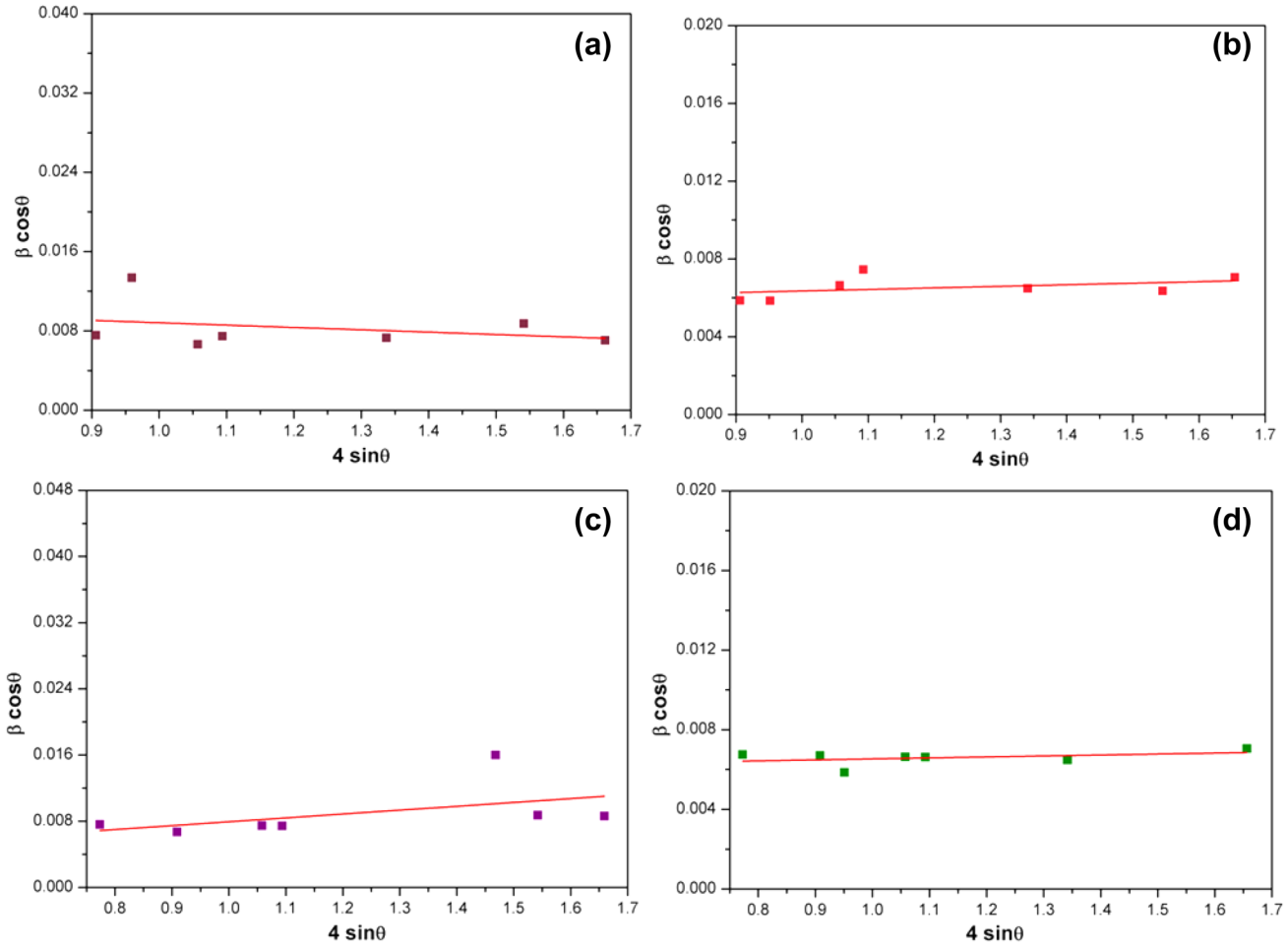

Fig. 3 W-H plots of $SnS_{1-x}Se_x$ films deposited at: **a** $T_s = 200$ °C, **b** $T_s = 250$ °C, **c** $T_s = 300$ °C and **d** $T_s = 350$ °C

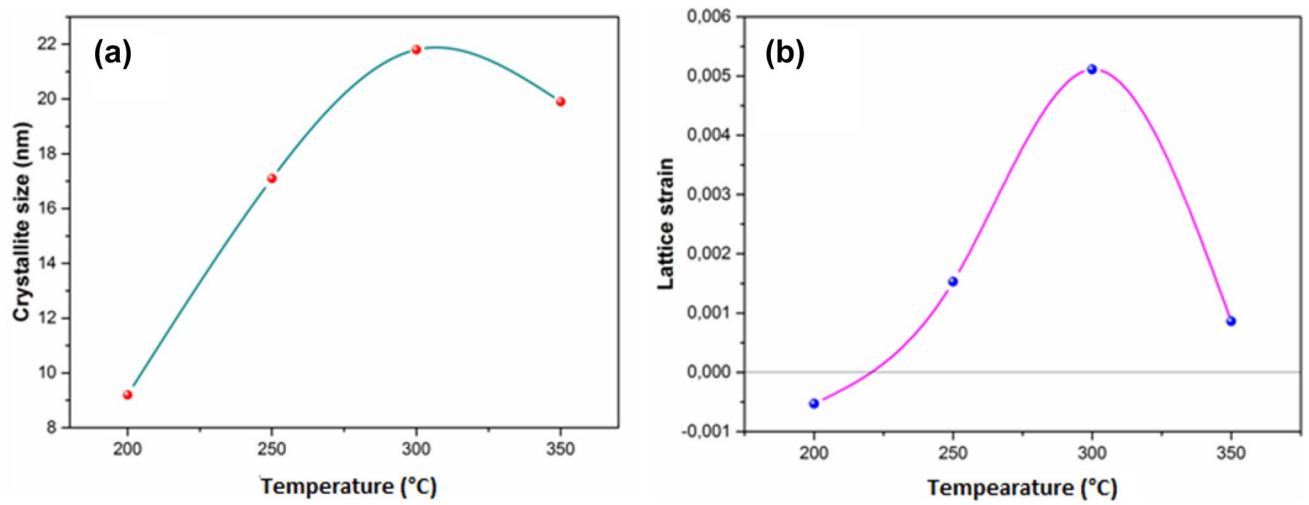

Fig. 4 Variation of **a** crystallite size and **b** lattice strain with substrate temperatures

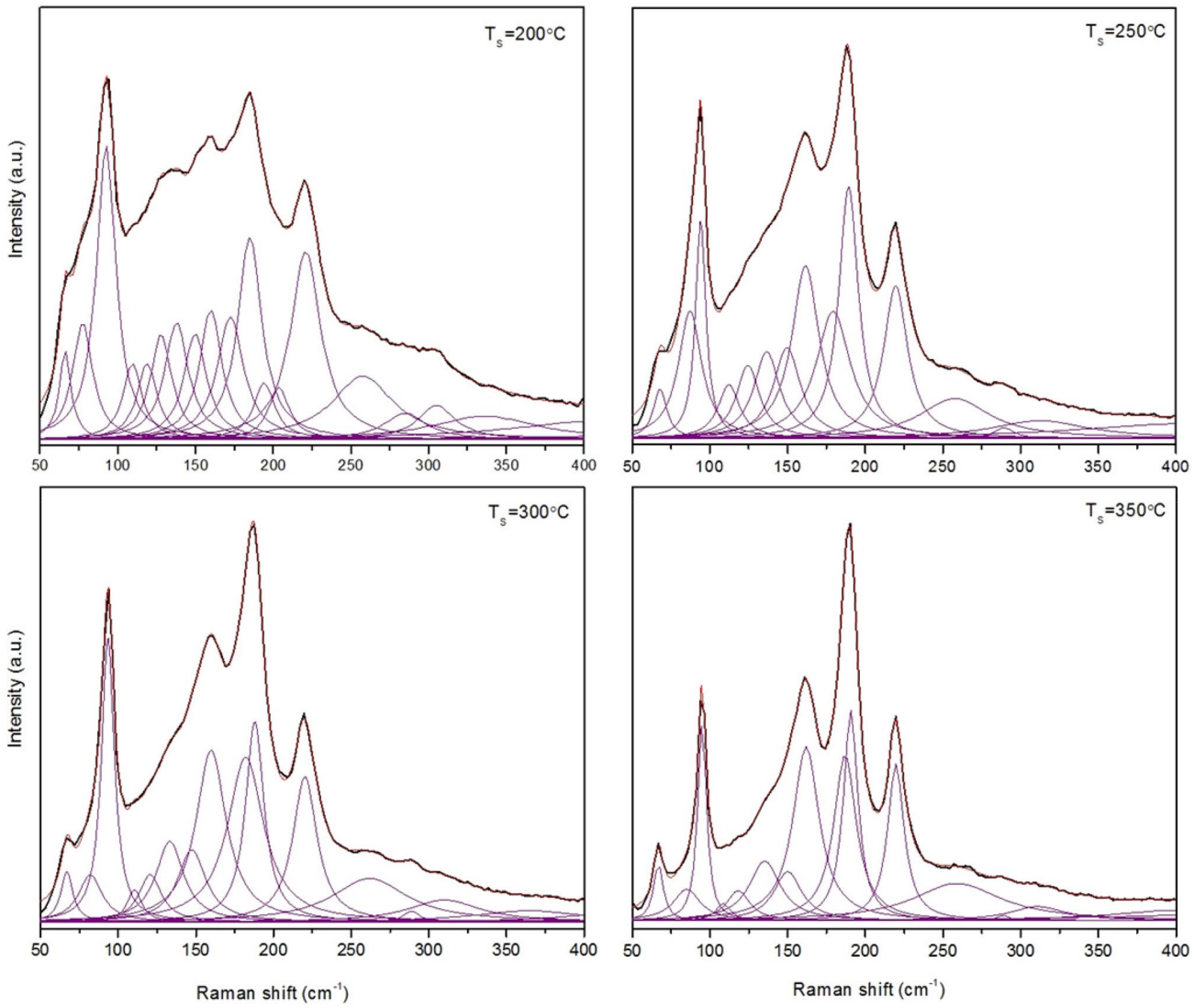

Fig. 5 Raman spectra of $SnS_{1-x}Se_x$ films deposited at different substrate temperatures

few broad peaks are observed, which are related to Sn_2S_3 and SnS_2 that are not observed in the GIXRD patterns. However, their intensity is insignificant, which indicates marginal presence of such phases in the films. Further, it could be seen from Fig. 5 that initially all the characteristic Raman modes of both SnS and SnSe are not clearly appeared, rather a mixture of different peaks appeared in the form of a broad peaks in the spectra. This appearance of broad peaks might be an indication of the mixed phase of SnS and SnSe. However, with increase of substrate temperature (with decrease of S content in the films as noted from Table 2), there is a clear appearance of Raman modes of SnS and SnSe with a symmetric shape. A similar trend of the appearance of broad peaks in $SnS_{1-x}Se_x$ ($0 \le x \le 1$) alloyed nanosheets was reported by Wei Gao et al. [29], who attributed this to the overlap of both SnS and SnSe peaks. Thomas Schnabel et al. [40] also observed a similar behaviour in $Cu_2ZnGeS_xSe_{4-x}$ films due to mixed sulfoselenide composition. Moreover, the intensity of Raman modes of $SnS_{1-x}Se_x$ films was increased with increase of substrate temperature and became sharp, indicating good crystallinity of the films grown at higher temperatures and these results were in agreement with the GIXRD data discussed earlier. Table 4 shows the observed Raman modes of $SnS_{1-x}Se_x$ films and the reported Raman modes of binary compounds of Sn and S/Se.

3.4 SEM analysis

Figure 6a–d shows the SEM pictures of $SnS_{1-x}Se_x$ layers deposited at different substrate temperatures. The SEM pictures clearly revealed a change in the shape and size of the grains with increase of substrate temperature. Also the

Table 4 Observed Raman modes of $SnS_{1-x}Se_x$ films deposited at different substrate temperatures

Observed Raman modes								Reported Raman modes				
$T_s = 200$ °C		$T_s = 250$ °C		$T_s = 300$ °C		$T_s = 350$ °C		SnS [41–45]	SnSe [46–48]	$SnSe_2$ [48]	Sn_2S_3 [41, 43]	SnS_2 [41, 43]
Peak position, cm^{-1}	FWHM, cm^{-1}	Peak position, cm^{-1}	FWHM, cm^{-1}	Peak position, cm^{-1}	FWHM, cm^{-1}	Peak position, cm^{-1}	FWHM, cm^{-1}	Peak position, cm^{-1}				
65.9	9.1	67.9	10.4	67.0	9.3	66.8	7.3	69	–	–	70	
77.2	15.4	–	–	–		–	–	–	75	–	–	
–	–	87.2	18.0	82.1	18.7	85.0	20.9	90	–	–	–	
92.3	15.1	94.1	8.1	93.5	10.0	94.9	6.5	95/97	–	–	–	
109.2	14.8	112.3	16.8	110.5	11.4	108.4	11.5	112	106-110	–	–	
118.6	15.6	–	–	120.6	17.7	118.1	18.0			119	–	
127.6	16.7	124.5	18.2	–	–	–	–	123	127NP	–	–	
137.6	18.5	136.6	20.2	133.3	21.7	135.2	24.2	–	133	–	–	
149.6	17.8	149.6	21.1	147.4	22.2	150.0	21.5	–	147/150	–	–	
159.6	17.5	161.6	21.4	159.9	23.6	161.9	20.4	160	–	–	–	
172.2	20.6	179.4	26.7	–	–	–	–	174/176	–	–	–	
184.7	18.8	–	–	182.1	28.1	187.0	17.4	183	187	185	–	
193.9	16.4	189.3	15.1	188.0	14.3	190.6	11.2	191	–	–	–	
203.5	15.9	–	–	–	–	–	–	202	–	–	–	
220.7	23.5	219.6	18.8	220.3	18.9	219.6	12.9	220	–	–	–	
257.4	47.8	257.6	55.1	262.0	59.1	259.8	69.1	250	–	–	–	
284.7	32.8	289.2	16.0	288.9	12.6	288.7	9.7	288	–	–	–	
305.3	29.0	312.4	76.5	310.0	56.6	311.0	43.5	–	–	–	307	312

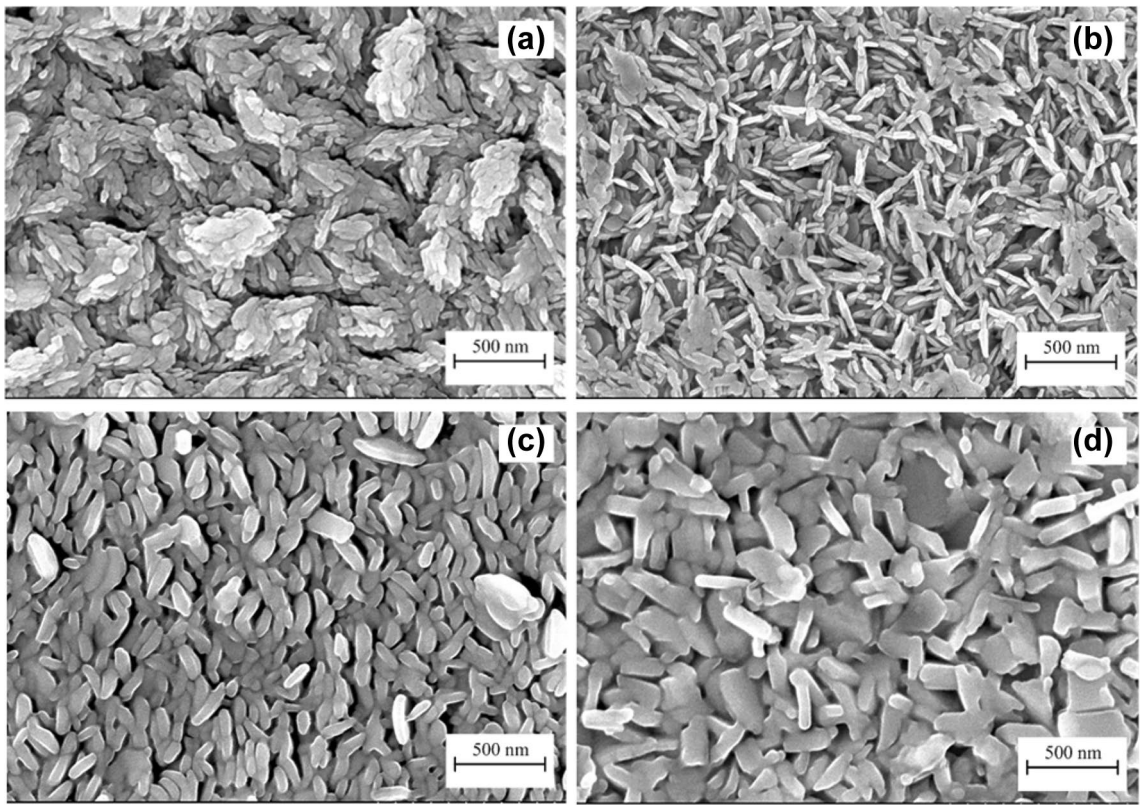

Fig. 6 SEM images of $SnS_{1-x}Se_x$ films deposited at: **a** $T_s = 200$ °C, **b** $T_s = 250$ °C, **c** $T_s = 300$ °C and **d** $T_s = 350$ °C

grains are uniformly distributed on the substrate surface. Initially, the films formed at $T_s = 200$ °C showed grains that are in bunches of cereal shape. Although the shape of cereal appeared big, it contained large number of smaller grains. With increase of substrate temperature to 250 °C, smaller grains in an individual cereal slowly grown into bigger size, resembling long-type rice grains. With further increase of temperature to 300 °C, the rice shaped grains grew horizontally along the width so that the grain bulges and turned into flake shape. In general, the increase in substrate temperature can influence the nucleation density that leads to the growth of nuclei into bigger size due to more surface diffusion of ad-atoms similar to Ostwald's ripening that occurs in solid solutions. With further increase of T_s to 350 °C, the edges of the flake shaped grains start melting and the adjacent grains coalescence together that leads to an increase in the flake size, indicating the recrystallization of grains at such temperatures. Also some grains remain in the same shape and size similar to that appeared at $T_s = 300$ °C. Further, the changes observed in the surface morphology of the films might be associated with the change in the composition of the films with substrate temperature. However, the layers formed at $T_s = 300$ °C showed uniform distribution of grains of similar shape and size on the substrate than the layers grown at other temperatures.

3.5 AFM analysis

Figure 7a–d shows the 2D AFM images of as-deposited $SnS_{1-x}Se_x$ films. The images were taken over an area of 5 μm × 5 μm. The images indicate that all the films were continuous. The grains were grown in different orientations, indicating the polycrystalline nature of the films. It can be seen from the pictures that the surface roughness was highly influenced by the substrate temperature. The various surface topographical parameters from the AFM data are also evaluated. Films grown at $T_s = 200$ °C showed higher surface roughness than films deposited at other temperatures. This might be due to the difference in the ad-atom incorporation kinetics because of the insufficient thermal energy at such low temperatures, which leads to high average surface roughness. Because of this, the incoming flux of atoms attach to the existing nuclei so that more hill-like structures have formed on the substrate surface at lower growth temperatures. Therefore, the films exhibited higher surface roughness at such temperatures. With increase of substrate temperature, the surface roughness was reduced with increased grain size. This might be because of the coalescence of smaller grains at higher temperatures, which results in lateral film formation on the substrate surface leading to larger grains [48].

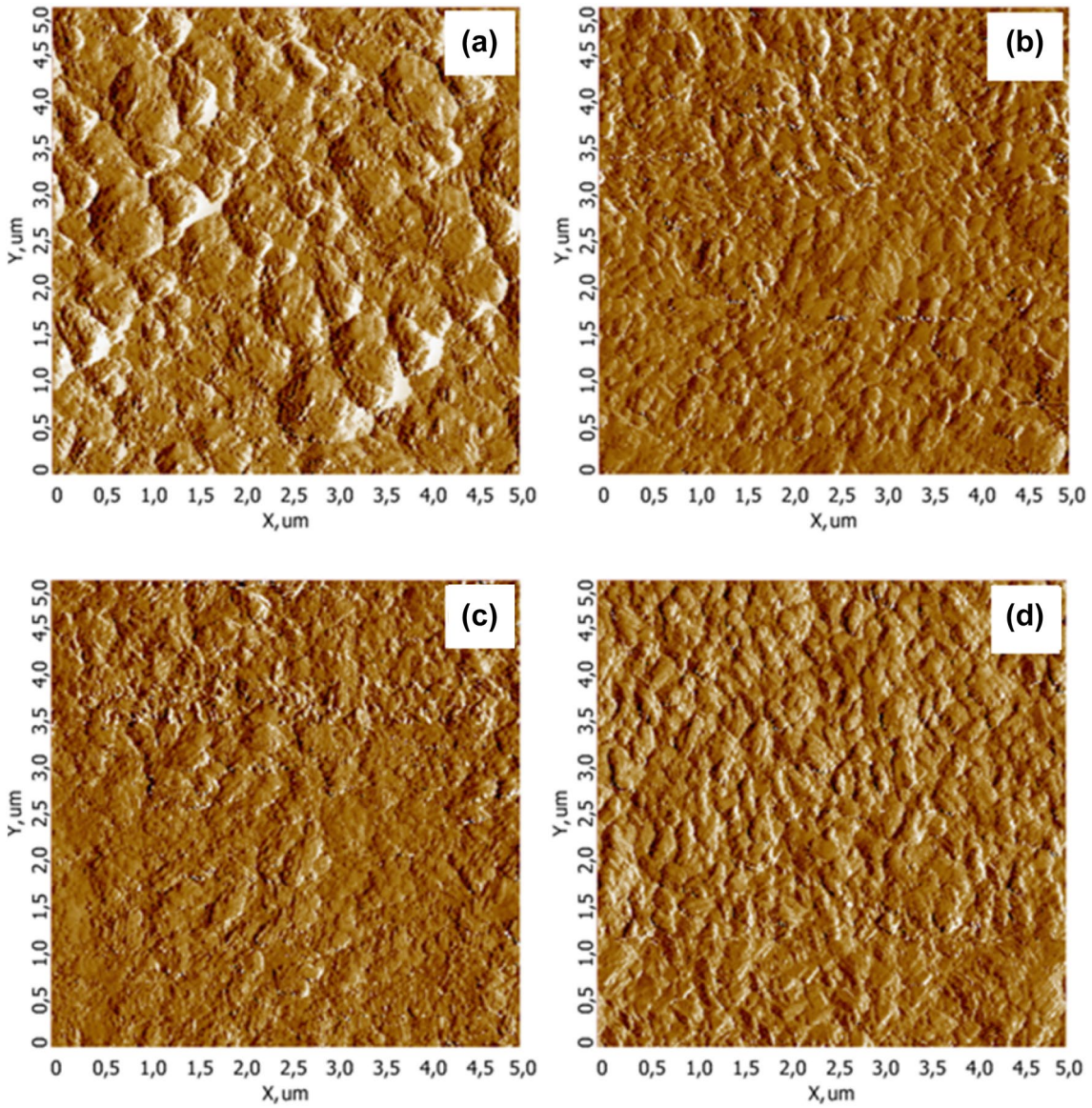

Fig. 7 2D AFM images and corresponding grain boundary images of $SnS_{1-x}Se_x$ films deposited at: **a** $T_s = 200$ °C, **b** $T_s = 250$ °C, **c** $T_s = 300$ °C and **d** $T_s = 350$ °C

The surface roughness parameters such as average roughness (R_a), root mean square roughness (R_q), skewness (R_{sk}) and kurtosis (R_{ku}) were estimated from the AFM data using NT-MDT spectrum instruments software and image analysis P9 processing module, while the average grain size (d) values were obtained using watershed method. Figure 8 shows the variation in roughness parameters with the substrate temperature of $SnS_{1-x}Se_x$ films. The average roughness and the RMS roughness of the as-deposited $SnS_{1-x}Se_x$ films were decreased and varied in the range, 36–22 nm and 45–27 nm respectively with increase of T_s, indicating growth of finest particles on the substrate at higher T_s values [50]. Further, the average grain size of the films was increased with increase of T_s as was observed in the SEM analysis. The skewness in the films was found to be positive and varied in the range, 0.5–0.2, indicating less distortion of peaks. This suggests a change from slightly asymmetric distribution of heights to symmetric distribution at higher T_s values [51]. In addition, kurtosis values were found to be > 3, implying the leptokurtic nature of the films with the appearance of highly intense and sharp peaks [52].

3.6 Photoconductance

The photoresponse of a material depends on the incident light intensity (L) and temperature of the specimen. The

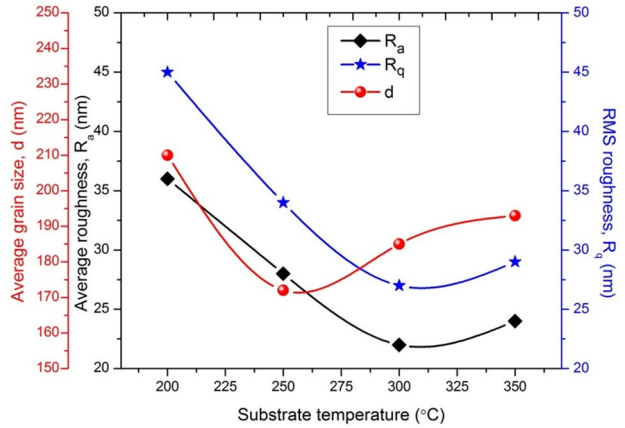

Fig. 8 Variation in roughness parameters (average roughness, RMS roughness and average grain size) with substrate temperature of $SnS_{1-x}Se_x$ films

response of as-deposited $SnS_{1-x}Se_x$ films to incident photons was examined using the photoconductance measurements carried out at a constant temperature. It can be determined by measuring the conductance of the films under light (σ_l) and dark (σ_d) conditions following the relation (5) [53],

$$\text{Photoresponse} = \frac{\sigma_l - \sigma_d}{\sigma_d} \tag{5}$$

Figure 9 shows the logarithm of photoresponse of the films with incident light intensity (L). The figure shows that the photoconductance was linearly increased with light intensity, which indicates an increased photo-generated charge carriers in the layers. A maximum photoresponse was observed for the films deposited at $T_s = 300$ °C. Generally, the photoresponse follows the power law with light intensity as L^{γ}, where γ value directly gives the type of carrier recombination either mono ($\gamma = 1$) or bimolecular ($\gamma = 0.5$) in the specimen [54]. The monomolecular recombination involves an electron in the conduction band recombines with a hole in the valance band via traps (energy levels) within the band gap region, which act as recombination centers. Therefore, this type of recombination is referred as trap assisted recombination process. On the other hand, the bimolecular recombination is a band to band recombination that occurs when an electron in the conduction band directly recombines with a hole in the valence band. In the present case, the γ values evaluated for $SnS_{1-x}Se_x$ films formed at $T_s = 200$, 250, 300 and 350 °C were 0.56, 0.40, 0.44 and 0.47 respectively. Thus, the γ values are ~ 0.5 for all the films, representing bimolecular type recombination of charge carriers through band-to-band transitions. Therefore, it is inferred from the above results that $SnS_{1-x}Se_x$ is a potential candidate for thin film solar cell application.

3.7 Optical analysis

The optical properties of $SnS_{1-x}Se_x$ films were measured in the wavelength range, 400–1400 nm. Figure 10 shows the optical absorbance spectra of $SnS_{1-x}Se_x$ films deposited at different T_s values. The spectra indicates that all the films had ~ 70% of absorbance in the visible region. Using the absorbance data, the absorption coefficient (α) of the films was determined and by assuming the direct allowed band-to-band transition in the films, the optical band gap energy (E_g) of the layers was evaluated by the following Tauc relation [54], where $h\nu$ is the incident photon energy and A is a constant.

$$(\alpha h\nu)^2 = A(h\nu - E_g) \tag{6}$$

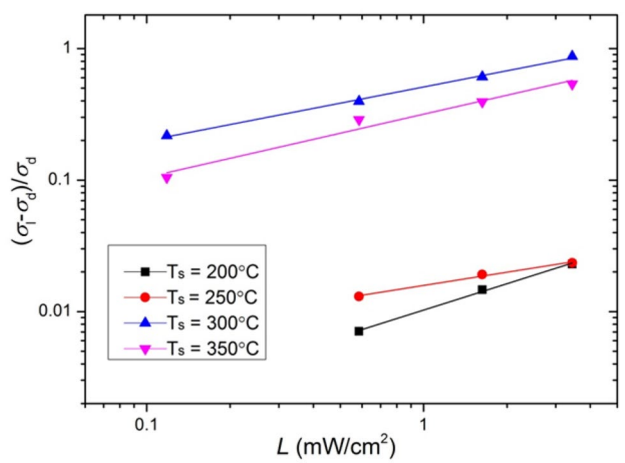

Fig. 9 Photoresponse of $SnS_{1-x}Se_x$ films with light intensity

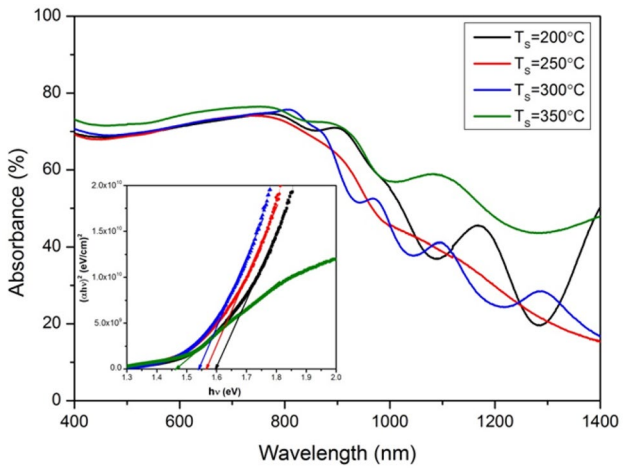

Fig. 10 Optical absorbance spectra of $SnS_{1-x}Se_x$ films

The $(\alpha h\nu)^2$ versus $h\nu$ plots of $SnS_{1-x}Se_x$ films are shown in inset of Fig. 10, from which the band gap energy of the layers can be evaluated by extrapolating the linear portion of the plots onto the energy axis. The determined E_g values of $SnS_{1-x}Se_x$ films were decreased from 1.59 to 1.46 eV with increase of T_s values. The decrease in band gap energy of the films is due to variation in composition leading to the appearance of different phases and improvement in crystalline quality of the films [56].

4 Conclusion

$SnS_{1-x}Se_x$ alloy films were deposited on glass substrates by co-evaporation of SnS and Se precursors at different substrate temperatures that varied in the range, 200–350 °C. The effect of substrate temperature on composition, structure, surface morphology, topography, photoresponse and optical properties of $SnS_{1-x}Se_x$ films was investigated. The EDS analysis confirmed that the composition of $SnS_{1-x}Se_x$ films was varied with substrate temperature. The GIXRD analysis revealed the formation of polycrystalline $SnS_{1-x}Se_x$ films with (111) plane as preferred orientation exhibiting orthorhombic crystal structure. Further, crystallinity of the films was improved with rise of substrate temperature. Raman analysis also supported the GIXRD results with the appearance of characteristic Raman modes of different phases. The SEM analysis revealed that all the as-deposited films were uniformly coated over the substrate surface and the grains appeared in different shapes as T_s increases. The AFM analysis showed that average roughness of the films was decreased from 36 to 22 nm with increase of substrate temperature. The photoresponse measurements revealed that $SnS_{1-x}Se_x$ films are very sensitive to light and the recombination of carriers was found to be bimolecular type in the films. From the optical studies, the energy band gap of the layers was decreased from 1.59 to 1.46 eV with increase of T_s. From the above analysis, it is concluded that $SnS_{1-x}Se_x$ alloy films deposited at $T_s = 300$ °C showed better properties compared to those layers formed at other temperatures, which can be used as an absorber layer in thin film solar cells.

Acknowledgements The authors, Prof. K.T. Ramakrishna Reddy and Prof. M.S. Tivanov wish to acknowledge the Dept. of Science and Technology, Govt. of India (Grant no: DST/INT/BLR/P-30/2019) and the State Committee on Science and Technology of the Republic of Belarus. The authors of this work are grateful to Affiliate RDC "Belmicrosystems" JSC "INTEGRAL"—"INTEGRAL" Holding Managing Company for SEM studies.

References

1. A. Basak, A. Mondal, U.P. Singh, Impact of substrate temperature on the structural, optical and electrical properties of thermally evaporated SnS thin films. Mater. Sci. Semicond. Process. **56**, 381 (2016)
2. Malkeshakumar Patel, Abhijit Ray, Junction and back contact properties of spray-deposited M/SnS/In_2S_3/SnO_2:F/Glass (M = Cu, Graphite) devices: Considerations to improve photovoltaic performance. J. Electron. Mater. **44**, 558 (2015)
3. B. Ghosh, M. Das, P. Banerjee, S. Das, Fabrication of vacuum-evaporated SnS/CdS heterojunction for PV applications. Sol. Energy Mater. Sol. Cells **92**, 1099 (2008)
4. K.S. Urmila, T.A. Namitha, J. Rajani, R.R. Philip, B. Pradeep, Optoelectronic properties and Seebeck coefficient in SnSe thin films. J. Semicond. **37**, 093002 (2016)
5. E.B. Salgado, M.T.S. Nair, P.K. Nair, Thin films of n-type $SnSe_2$ produced from chemically deposited p- type SnSe. Thin Solid Films **598**, 149 (2016)
6. N.E. Makori, I.A. Amatalo, P.M. Karimi, W.K. Njoroge, Optical and electrical properties of SnSe thin films for solar cell applications. Am. J. Condens. Matter Phys. **4**, 87 (2014)
7. T.R. Rana, S.Y. Kim, J.H. Kim, Existence of multiple phases and defect states of SnS absorber and its detrimental effect on efficiency of SnS solar cell. Curr. Appl. Phys. **18**, 663 (2018)
8. Y. Takano, K. Oyaizu, Fabrication of SnS-MgSnO heterojunction solar cells using vacuum thermal evaporation and sol–gel method. Mater. Lett. **228**, 414 (2018)
9. T.M. Razykov, G.S. Boltaev, A. Bosio, B. Ergashev, K.M. Kouchkarov, N.K. Mamarasulov, A.A. Mavlonov, A. Romeo, N. Romeo, O.M. Tursunkulov, R. Yuldoshov, Characterization of SnSe thin films fabricated by chemical molecular beam deposition for use in thin film solar cells. Sol. Energy **159**, 834 (2018)
10. P. Sinsermsuksakul, L. Sun, S.W. Lee, H.H. Park, S.B. Kim, C. Yang, R.G. Gordon, Overcoming efficiency limitations of SnS-based solar cells. Adv. Energy Mater. **4**, 1400496 (2014)
11. N.E. Makori, I.A. Amatalo, P.M. Karimi, W.K. Njoroge, Characterization of SnSe/CdO: Sn P–N junction for solar cell applications. Int. J. Energy Eng. **5**, 1 (2015)
12. W. Shockley, H.J. Queisser, Detailed balance limit of efficiency of p–n junction solar cells. J. Appl. Phys. **32**, 510 (1961)
13. Y. Wei, D. Zhuang, M. Zhao, W. Zhang, G. Ren, Y. Wu, R. Sun, Q. Gong, L. Zhang, S. Zhan, X. Peng, X. Lyu, Beyond 10% efficient CZTSSe thin film solar cells fabricated by a two-step CdS deposition process. Sol. Energy Mater. Sol. Cells **180**, 19 (2018)
14. W. Albers, C. Haas, H. Ober, G.R. Schodder, J.D. Wasscher, Preparation and properties of mixed crystals $SnS_{(1-x)}Se_x$. J. Phys. Chem. Solids **23**, 215 (1962)
15. T.H. Patel, R. Vaidya, S.G. Patel, Anisotropic behaviour of semiconducting tin monosulphoselenide single crystals. Bull. Mater. Sci. **26**, 569 (2003)
16. B. Subramanian, C. Sanjeeviraja, M. Jayachandran, Materials properties of electrodeposited $SnS_{0.5}Se_{0.5}$ films and characterization of photoelectrochemical solar cells. Mater. Res. Bull. **38**, 899 (2003)
17. H. Wei, Y. Su, S. Chen, Y. Lin, Z. Yang, X. Chen, Y. Zhang, Novel SnS_xSe_{1-x} nanocrystals with tunable band gap: experimental and first principles calculations. J. Mater. Chem. **21**, 12605 (2011)
18. T. Mahalingam, V. Danasekaran, G. Ravi, R. Chandramohan, A. Kathalingam, J.K. Rhee, Role of deposition potential on the optical properties of SnSSe thin;films. ECS Trans. **35**, 1 (2011)
19. H.S. Im, Y. Myung, Y.J. Cho, C.H. Kim, H.S. Kim, S.H. Back, C.S. Jung, D.M. Jang, Y.R. Lim, J. Park, J.P. Ahn, Facile phase and composition tuned synthesis of tin chalcogenide nanocrystals. RSC Adv. **3**, 10349 (2013)

20. V. Dhanasekaran, K. Sundaram, J. Jung, T. Mahalingam, Microstructural properties evaluation of SnSSe alloy films. J. Mater. Sci.: Mater. Electron., **26**, 1641 (2015)
21. E. Barrios-Salgado, L.A. Rodriguez-Guadarrama, A.R. Garcia-Angelmo, J.C. Alvarez, M.T.S. Nair, P.K. Nair, Large cubic tin sulphide-tin selenide thin film stacks for energy conversion. Thin Solid Films **615**, 415 (2016)
22. H. Ju, M. Kim, D. Park, J. Kim, A strategy for low thermal conductivity and enhanced thermoelectric performance in SnSe: porous $SnSe_{1-x}S_x$ nanosheets. Chem. Mater. **29**, 3228 (2017)
23. T.T. Ly, G. Duvjir, T. Min, J. Byun, T. Kim, M.M. Saad, N.T.M. Hai, S. Cho, J. Lee, J. Kim, Atomistic study of the alloying behaviour of crystalline $SnSe_{1-x}S_x$. Phys. Chem. Chem. Phys. **19**, 21648 (2017)
24. T.R. Asfandiyar, A. Wei, F.H. Li, Y. Sun, C.F. Pan, M.U. Wu, H. Farooq, F. Tang, B. Li, J.F. Li, Li, Thermoelectric SnS and SnS-SnSe solid solutions prepared mechanical alloying and spark plasma sintering: anisotropic thermoelectric properties. Sci. Rep. **7**, 1 (2017)
25. E. Barrios-Salgado, L.A. Rodriguez-Guadarrama, M.L.R. Garcia, L.G. Martinez, M.T.S. Nair, P.K. Nair, Thin film solar cells of cubic structured SnS-SnSe. Phys. Status Solidi A **1700036**, 1 (2017)
26. H. Kafashan, M. Azizieh, Z. Balak, Electrochemical synthesis of nanostructured Se-doped SnS: effect of Se-dopant on surface characterizations. Appl. Surf. Sci. **410**, 186 (2017)
27. H. Ju, K. Kim, D. Park, J. Kim, Fabrication of porous SnSeS nanosheets with controlled porosity and their enhanced thermoelectric performance. Chem. Engg. J. **335**, 560 (2018)
28. A. Ektarawong, B. Alling, Stability of $SnSe_{1-x}S_x$ solid solutions revealed by first-principles cluster expansion. J. Phys.: Condens. Matter **30**, 29LT01 (2018)
29. W. Gao, Y. Li, J. Guo, M. Ni, M. Liao, H. Mo, J. Li, Narrow-gap physical vapour deposition synthesis of ultrathin $SnS_{1-x}Se_x$ ($0 \le x \le 1$) two-dimensional alloys with unique polarized Raman spectra and high (opto)electronic properties. Nanoscale **10**, 8787 (2018)
30. V. Kumar, D.K. Sharma, K. Sharma, P. Singh, D.K. Dwivedi, Preparation and characterization of screen printed $SnS_{0.5}Se_{0.5}$ alloy films. J. Mater. Sci.: Mater. Electron. **29**, 846 (2018)
31. A. Banotra, N. Padha, Development of $SnS_{0.4}Se_{0.6}$ ternary alloy on annealing of thermally deposited films. J. Electron. Mater. **47**, 1 (2018)
32. H. Kafashan, Comparison the effects of Se and Te inclusion on the physical and electrochemical properties of SnS thin films. Mater. Sci. Semicond. Process. **88**, 148 (2018)
33. M. Parlak, C. Ercelebi, The effect of substrate and post-annealing temperature on the structural and optical properties of polycrystalline InSe thin films. Thin Solid Films **322**, 334 (1998)
34. K.T.R. Reddy, Y.V. Subbaiah, T.B.S. Reddy, D. Johnston, I. Forbes, R.W. Miles, Pyrolytic spray deposition of ZnS_xSe_{1-x} layers for photovoltaic applications. Thin Solid Films **431–432**, 340 (2003)
35. D. Nithyaprakash, P. Maadeswaran, J. Chankdrasekaran, M. Ramamurthy, Effect of substrate temperature on structural, optical and thermal properties of chemically sprayed ZnS thin films. J. Optoelectron. Adv. Mater. **12**, 2069 (2010)
36. Z.Y. Zhong, E.S. Cho, S.J. Kwon, Effect of substrate temperatures on evaporated In2S3 thin film buffer layers for Cu(In, Ga)Se2 solar cells. Thin Solid Films **547**, 22 (2013)
37. Y.M. Han, J. Zhao, M. Zhou, X.X. Jiang, H.Q. Leng, L.F. Li, Thermoelectric performance of SnS and SnS–SnSe solid solution. J. Mater. Chem. A **3**, 4555 (2015)
38. H. Kafashan, X-ray diffraction line profile analysis of undoped and Se-doped SnS thin films using Scherrer's, Williamson–Hall and size–strain plot methods. J. Electron. Mater. **48**, 1294 (2019)
39. N. Revathi, P. Pratap, Y.P.V. Subbaiah, K.T. Ramakrishna Reddy, Substrate temperature dependent physical properties of In_2S_3 films. J. Phys. D: Appl. Phys. **41**, 155404 (2008)
40. T. Schnabel, M. Seboui, E. Ahlswede, Band gap tuning of $Cu_2ZnGeS_xSe_{4-x}$ absorbers for thin-film solar cells. Energies **10**, 1813 (2017)
41. L. Zhao, Y. Di, C. Yan, F. Liu, Z. Cheng, L. Jiang, X. Hao, Y. Lai, J. Li, Insitu growth of SnS absorbing layer by reactive sputtering for thin film solar cells. RSC Adv. **6**, 4108 (2016)
42. R.E. Abutbul, E. Segev, L. Zeiri, V. Ezersky, G. Makov, Y. Golan, Synthesis and properties of nanocrystalline π-SnS—a new cubic phase of tin sulphide. RSC Adv. **6**, 5848 (2016)
43. J.M. Skelton, L.A. Burton, A.J. Jackson, F. Oba, S.C. Parker, A. Walsh, Lattice dynamics of the tin sulphides SnS_2, SnS and Sn_2S_3: vibrational spectra and thermal transport. Phys. Chem. Chem. Phys. **19**, 12452 (2017)
44. M. Steichen, R. Djemour, L. Gutay, J. Guillot, S. Siebentritt, P.J. Dale, Direct synthesis of single-phase p-type SnS by electrodeposition from a dicyanamide ionic liquid at high temperature for thin film solar cells. J. Phys. Chem. C **117**, 4383 (2013)
45. S. Sohila, M. Rajalakshmi, C. Ghosh, A.K. Arora, C. Muthamizhchelvan, Optical and Raman scattering studies on SnS nanoparticles. J. Alloy. Comp. **509**, 5843 (2011)
46. R.E. Abutbul, E. Segev, S. Samuha, L. Zeiri, V. Ezersky, G. Makov, Y. Golan, A new nanocrystalline binary phase: synthesis and properties of cubic tin monoselenide. CrystEngComm **18**, 1918 (2016)
47. X. Xu, Q. Song, H. Wang, P. Li, K. Zhang, Y. Wang, K. Yuan, Z. Yang, Y. Ye, L. Dai, In-plane anisotropies of polarized Raman response and electrical conductivity in layered tin selenide. ACS Appl. Mater. Interfaces. **9**, 12601 (2017)
48. P.A. Fernandes, M.G. Sousa, P.M.P. Salome, J.P. Leitao, A.F. Da Cunha, Thermodynamic pathway for the formation of SnSe and $SnSe_2$ polycrystalline thin films by selenization of metal precursors. CrystEngComm **15**, 10278 (2013)
49. T. Sall, B.M. Soucase, M. Mollar, B. Hartitti, M. Fahoume, Chemical spray pyrolysis of β-In_2S_3 thin films deposited at different temperatures. J. Phys. Chem. Solids **76**, 100 (2015)
50. A. Kassim, H.S. Min, A. Sharif, J. Haron, S. Nagalingam, Chemical bath deposition of SnS thin films: AFM, EDAX and UV-Visible characterization. Oriental J. Chem. **27**, 1375 (2011)
51. K. Wysocka, A. Ulatowska-Jarza, J. Bauer, I. Holowacz, B. Savu, G. Stanciu, H. Podbielska, AFM examination of sol-gel matrices doped with photosensitizers. Opt. Appl. **38**, 127 (2008)
52. E.S. Gadelmawla, M.M. Koura, T.M.A. Maksoud, I.M. Elewa, H.H. Soliman, Roughness parameters. J. Mater. Proces. Tech. **123**, 133 (2002)
53. S. Mahato, A.K. Kar, The effect of annealing on structural, optical and photosensitive properties of electrodeposited cadmium selenide thin films. J. Sci. Adv. Mater. Devices **2**, 165 (2017)
54. Neetu, M. Zulfequar, Photoconductivity of $Se_{90-x}Te_{10}Zn_x$ thin films. Indian J. Pure Appl. Phys. **52**, 53 (2014)
55. J. Tauc, *Optical properties of solids* (North-Holland, Amsterdam, 1970), p. 903
56. L. Zhao, Y. Di, C. Yan, F. Liu, Z. Cheng, L. Jiang, X. Hao, Y. Lai, J. Li, In situ growth of SnS absorbing layer by reactive sputtering for thin film solar cells. RSC Adv. **6**, 4108 (2016)